Infrared Spectroscopy on Electronic Structures of Platinum-group Metal Pernitrides MN_2 (M = Ru, Rh, Ir, and Pt)

Kazuo Soda[a,b,1*], Mai Komabuchi[a], Keisuke Maeguchi[c], Masahiko Kato[a,1], Toshiki Terabe[d], Ken Niwa[d,1], Masashi Hasegawa[d,1], Yuka Ikemoto[e], and Hidekazu Okamura[f]

[a]*Department of Quantum Engineering, Graduate School of Engineering, Nagoya University, Furo-cho, Chikusa-ku, Nagoya 464-8603, Japan*

[b]*Synchrotron Radiation Research Center, Nagoya University, Furo-cho, Chikusa-ku, Nagoya 464-8603, Japan*

[c]*Department of Materials Physics, Graduate School of Engineering, Nagoya University, Furo-cho, Chikusa-ku, Nagoya 464-8603, Japan*

[d]*Department of Crystalline Materials Engineering, School of Engineering, Nagoya University, Furo-cho, Chikusa-ku, Nagoya 464-8603, Japan*

[e]*Japan Synchrotron Radiation Research Institute, 1-1-1 Kouto, Sayo-cho, Sayo-gun, Hyogo 679-5198, Japan*

[f]*Department of Chemical Science and Technology, Faculty of Engineering, Tokushima University, 2-1 Minamijyousanjima-cho, Tokushima 770-8506, Japan*

(Received)

The electronic structures of platinum-group metal pernitrides MN_2 (M = Ru, Rh, Ir, and Pt) were investigated via synchrotron radiation infrared spectroscopy and first-principles calculations. Measured reflectance spectra of marcasite-type RuN_2 and RhN_2 showed Drude-like responses, approaching 1 as the photon energy was decreased, whereas reflectance of arsenopyrite-type IrN_2 and pyrite-type PtN_2 became ~0.3 in the low photon energy region with a few features. These findings agreed well with the predictions of the metallic nature of marcasite-type RuN_2 and RhN_2 and the semiconducting properties of arsenopyrite-type IrN_2 and pyrite-type PtN_2, respectively. The measured reflectance spectra were also reasonably consistent with the calculated optical responses. The band gaps of IrN_2 and PtN_2 were estimated to be 0.8 and 2.1 eV, respectively, via first-principles calculation with a modified Becke–Johnson (MBJ) potential for the exchange potential.

Key words: infrared reflectance spectra, first-principles calculation, platinum-group metal pernitride, valence band electronic structure

1. Introduction

Recently, metal nitrides have attracted much attention as new wide bandgap semiconductors, high dielectric insulators, superhard materials, and good thermal conductors [1]. Late transition metal (TM) nitrides are also interesting as the counterparts of TM oxides; TM oxides show fascinating magnetic and electric properties due to the competitive localized and itinerant nature of their strongly correlated TM 3*d* electrons [2]. Furthermore, the large spin-orbit interaction in 4*d* and 5*d* late TM compounds may bring new material families such as Weyl semimetals [3-5], topological insulators and superconductors [6,7]. Although platinum-group metals, i.e., late 4*d* and 5*d* TMs, cannot easily form nitrides due to the stable triple-bonded nitrogen molecules under normal conditions, their pernitrides can be produced via direct reactions with supercritical nitrogen fluid under extremely high pressure and temperature [8-12]. These pernitrides are found to have relatively large bulk moduli; for example, the bulk modulus of arsenopyrite-type IrN_2 is comparable to that of diamond [12]. However, because the pernitirides formed in a laser-heated diamond anvil cell (LH-DAC) are very small, their electric and magnetic properties are not so well characterized yet. According to first-principles calculations reported to date [11,13-15], marcasite-type RuN_2 and RhN_2 are predicted to have metallic electronic band structures, whereas arsenopyrite-type IrN_2 and pyrite-type PtN_2 are expected to show insulating electronic band structures with predicted indirect gaps of E_G = 0.4 and 1.5 eV, respectively. These electronic structures have been partly confirmed by microbeam hard X-ray photoelectron spectroscopy [16] for the occupied electronic states of RuN_2, IrN_2, and PtN_2, which can be recovered to ambient pressure without suffering decomposition and structural phase transitions. For marcasite-type RhN_2, the observation of weak Raman signals due to the N_2 unit in the marcasite structure [9], which is often believed to indicate the insulating property [12], is inconsistent with the predicted metallic electronic band structure [13,15]. In exploring new materials and understanding their physical properties for the basic research and application, it is important to investigate their electronic band structures not only for the occupied states but also for the unoccupied states.

To clarify the electronic structures and electric properties of marcasite-type RuN_2 and RhN_2, arsenopyrite-type IrN_2, and pyrite-type PtN_2, this study reports the results of synchrotron radiation infrared (IR) spectroscopy and related first-principles calculation. IR reflectance spectra exhibit characteristic features depending on the metallic or insulating (semiconducting) electronic band structures, as well as the vibrational (phonon) and electronic excitations. Synchrotron radiation as a bright IR photon source enables us to study the

electronic structure at both ambient pressure and high pressure [17].

2. Experimental and Calculation Details

Synchrotron radiation IR spectroscopy was performed with the beamline BL43IR at SPring-8, an 8-GeV synchrotron radiation facility in Japan [17]. IR reflectance spectra were typically recorded between photon energies ($\hbar\omega$) of 0.01 and 1.9 eV at room temperature using microscopes (BRUKER Hyperion 2000 or custom-made long-working-distance microscope), Fourier-transform IR (FTIR) spectrometers (BRUKER Vertex70 or IFS120HR), and a Si-bolometer or HgCdTe detector. The probing beam size was approximately 0.03 mm in diameter for the photon energy higher than ~0.1 eV, while it was approximately 0.05 to 0.1 mm for the lower photon energy, depending on the photon energy. Pernitride specimens of RuN_2, RhN_2, IrN_2, and PtN_2 in typical size of ~0.1 mm in diameter were synthesized under extremely high pressure and temperature in an LH-DAC via a direct reaction of platinum-group metal with supercritical nitrogen fluid. The formation of the pernitrides was confirmed by their characteristic Raman spectra and/or X-ray diffraction patterns. Details of the synthesizing procedures and conditions are described in the literature [8,9,16]. As shown in Fig.1, the synthesized specimens were placed in the DAC, in which one of the two diamond anvils was of type IIa to transmit the probing infrared photons, and then the DAC was filled with nitrogen (as synthesized) or some other pressure-transmitting medium, such as NaCl (after once recovered to ambient pressure), for the IR reflectance measurements under various pressures. Although uniaxial effects such as broadening of the features might be anticipated for use of the NaCl pressure-transmitting medium, we did not recognize such effects in the present research; a quasi-hydrostatic condition may be held with the NaCl medium, since NaCl is much softer than the presently-investigated superhard pernitrides. A small ruby ball (not indicated in the figure) was also mounted as a pressure gauge for ruby fluorescence measurements [17-19], and reference Au was placed alongside the pernitride specimen between a stainless steel gasket and the diamond anvil. Reflectance spectra at ambient pressure were also measured for RuN_2, IrN_2, and PtN_2; these pernitride specimens were recovered to ambient pressure and placed on a glass plate together with a reference Au foil. RhN_2 specimens were kept in the DAC under high pressures since RhN_2 decomposed into small grains at ambient pressure [9]. IR reflectance spectra were obtained by averaging the spectra measured at several points of the specimens and dividing them by the metallic reference Au spectra.

First-principle calculations within the density functional theory (DFT) scheme were performed using a full-potential linearized augmented plane wave method in a generalized gradient approximation (GGA–PBE) [20] with the WIEN2k code [21,22] for the nonmagnetic states of all the investigated pernitrides with their experimental lattice parameters [8,9,16]. The lattice constants used in the present calculation are listed in Table 1 with their bulk moduli. We employed 1000 *k* points in the Brillouin zone for a self-consistent field cycle, the parameter of $R_{MT}K_{max} = 7$, and a cutoff energy of ~400 eV. In the present calculation for the optical properties, the spin-orbit interaction was neglected as a first step. The inclusion of the spin-orbit interaction is beyond the present scope, although it may bring splitting and intensity reduction of bands [16] and additional features in the optical spectra [23]. The reflectance spectra were calculated with a module of the WIEN2k code [24] for comparison with the measured spectra. In the calculation, the interband contribution to the imaginary part ε_2 of the complex dielectric function $\tilde{\varepsilon} = \varepsilon_1 + i\varepsilon_2$ was evaluated within the random-phase approximation, whereas its real part ε_1 was obtained using the Kramers–Kronig relation [24]. The integration of the Kramers–Kronig formula was performed up to a cut-off energy. For the intra-band contribution of free carriers in metals, the associated plasmon energy $\hbar\omega_p$ was estimated in the WIEN2k code [23], which gives its complex dielectric function: $\tilde{\varepsilon} = 1 - \{(\hbar\omega_p)^2/[(\hbar\omega)^2 + i\hbar\omega\hbar\gamma]\}$. Here, a lifetime broadening (scattering rate) $\hbar\gamma$ was assumed to be 0.1 – 0.3 eV, which may be typical values derived from electric conductivities of metals. From the calculated complex dielectric function, the optical constants (refractive index *n* and extinction coefficient κ) in the expression of the complex refractive index $\tilde{n} = n + i\kappa = \sqrt{\tilde{\varepsilon}}$ were estimated; then, the reflectance *R* was calculated by the following relation [17,23,25]: $R = |(\tilde{n} - n_0)/(\tilde{n} + n_0)|^2$, where n_0 is the refractive index of the medium, $n_0 = 1$ for vacuum and air and $n_0 = 2.4$ for DAC [17]. We also estimated the band gap E_G of arsenopyrite-type IrN_2 and pyrite-type PtN_2 using the modified version of the exchange potential proposed by Becke and Johnson (MBJ) [26] instead of the GGA–PBE potential to improve the predicted value of the band gap.

3. Results and Discussion

Figure 2 shows the measured reflectance spectra of marcasite-type RuN_2, arsenopyrite-type IrN_2, and pyrite-type PtN_2 at ambient pressure (solid curves) in comparison with calculated reflectance spectra (broken curves). The calculated spectra were obtained by averaging the

reflectance spectra for three polarization directions of the orthorhombic marcasite-type and monoclinic arsenopyrite-type structures. Typical errors are indicated for RuN_2 in the figure, estimated from deviations in several measurements at various points of specimens. Small dips observed between $\hbar\omega$ values of 0.2 and 0.3 eV were due to the defect and/or impurity absorption of a diamond window in the optical path of BL43IR [17]. The reflectance of marcasite-type RuN_2 increased to ~1 as the photon energy decreased in the low photon energy, i.e., it exhibited a Drude-like response due to free carriers. This was consistent with the metallic band structure predicted for marcasite-type RuN_2. For pyrite-type PtN_2 and arsenopyrite-type IrN_2, the reflectance stayed low at ~0.3 in the low photon energy region, which indicated the insulating (semiconducting) nature of these pernitrides. Photon energies corresponding to the predicted indirect band gaps are indicated by arrows for arsenopyrite-type IrN_2 and pyrite-type PtN_2 in the figure. Since it is well known that the DFT–GGA–PBE calculation tends to underestimate the band gap value, we performed the DFT–MBJ calculation [26], which predicts band gap energies of 0.8 and 2.1 eV for arsenopyrite-type IrN_2 and pyrite-type PtN_2, respectively. The origin of the large feature observed around 0.4 eV for PtN_2 is unclear at present. Since recent hard X-ray photoelectron spectroscopy [16] shows the existence of an unreacted Pt metal under PtN_2 and the Fermi level pinning for the semiconducting PtN_2, which suggests the existence of the mid-gap states probably at their interface, we speculate that the large feature might be partly attributed to the in-gap states or related to the residual metallic component. Although further experimental study of the optical properties in the higher photon energy region is required for clarifying the band gap energies of arsenopyrite-type IrN_2 and pyrite-type PtN_2, a small hump around $\hbar\omega$ = 1.4 eV for PtN_2 and a shoulder around 1.3 eV for IrN_2 might imply that the features are related to the interband transitions.

Here, we briefly discuss the change in the electronic structures calculated using the MBJ potential in comparison with the DFT–GGA–PBE calculation. Calculated densities of states (DOSs) of arsenopyrite-type IrN_2 and pyrite-type PtN_2 are shown in Fig. 3 (a) and (b), respectively. In the figure, hard X-ray photoelectron spectra, reported in the literature [16], are also presented for comparison. The origin of the binding energy is set to the experimental Fermi edge of a reference Au [16], and the calculated DOSs are plotted so that the occupied valence-band tops and the centers of the band gaps are aligned to the Fermi energy for IrN_2 and PtN_2, respectively, because the experimental spectra show the p-type semiconducting feature for IrN_2 and the starting metallic Pt contribution near the Fermi energy for PtN_2 [16].

In the DOS calculated using the MBJ potential for both IrN_2 and PtN_2, the following trends are found; (1) the overall widths of the valence bands are almost the same but rather slightly narrower than the DFT–GGA results; (2) the shallow antibonding N 2s-derived bands are located deeper and agree much better with the experimental results than the DFT–GGA calculations; (3) the unoccupied conduction bands are located much higher than the DFT–GGA predictions, as reported for Si [26]. Thus, the conduction band shift in the DFT–MBJ calculation is the main origin of the increase in the predicted band gap value. In turn, the photon energy positions of the optical features are probably underestimated in the DFT-GGA calculation.

In Fig. 4, experimentally observed IR reflectance spectra (solid curves) of marcasite-type RuN_2 and RhN_2 under high pressures of 28 and 33 GPa, respectively, in DAC are compared with their spectra (broken curves) calculated with n_0 = 2.4 and lattice parameters at 43 GPa. Large dip features induced by the defect and/or impurity in type IIa DAC are observed around $\hbar\omega$ = 0.2–0.3 eV. To compensate for these dip features, we fitted Drude–Lorentz model response functions to the experimental spectra below $\hbar\omega \approx 1$ eV [17,27], as shown by gray curves in the figure. Here, the complex dielectric function is expressed by

$$\tilde{\varepsilon} = \varepsilon_\infty - \frac{\left(\hbar\omega_{\mathrm{PD}}\right)^2}{\left(\hbar\omega\right)^2 + i\hbar\omega\hbar\gamma_{\mathrm{D}}} + \frac{\left(\hbar\omega_{\mathrm{PL}}\right)^2}{\left(\hbar\omega_0\right)^2 - \left(\hbar\omega\right)^2 - i\hbar\omega\hbar\gamma_{\mathrm{L}}}, \qquad (1)$$

where the first term ε_∞ represents the contribution from the higher-energy interband transitions, and the second and third terms denote a free carrier (Drude) contribution (plasmon energy $\hbar\omega_{\mathrm{PD}}$ and scattering rate γ_{D}) and a bound electron (Lorentz) contribution (eigenenergy corresponding to an optical transition $\hbar\omega_0$, its linewidth $\hbar\gamma_{\mathrm{L}}$, and plasma energy $\hbar\omega_{\mathrm{PL}}$), respectively. These fitting parameters are listed in Table 2. Dotted curves represent the absorption spectra obtained from a relation between the extinction coefficient κ and the absorption coefficient $\alpha \propto \kappa\hbar\omega$ with the calculated extinction coefficients κ averaged over polarization. Compared to the IR spectra in the air (n_0 = 1; shown in Fig. 2 for RuN_2), the reflectance is reduced in the high photon energy region. Both the measured reflectance spectra nearly reached 1 in the low photon energy region, which agreed qualitatively with their predicted metallic band structures.

For detailed comparison, Fig. 5 shows the DOSs calculated for marcasite-type RuN_2 under ambient pressure and high pressure of 28 GPa and for RhN_2 under high pressure of 35 GPa. A hump structure around $\hbar\omega$ = 2 eV in the calculated IR spectra is attributed to the transition

from the valence-band Ru *d* (*p*) states around the binding energy E_B = 1 eV to the conduction-band Ru *p* (*d*) states at $E_B \approx -1$ eV, which corresponds to the shoulder structure at $\hbar\omega$ = 2 eV in the absorption spectrum of marcasite-type RuN_2. As seen in Figs. 2 and 4, the hump structure slightly shifted toward the high photon energy when the pressure increased. This can be explained by the pressure-dependence of the widths and positions of the relevant valence and conduction bands. As seen in Fig. 5, for marcasite-type RuN_2, the band widths became large under high pressures since the interactions between the constituent atoms are increased by the reduced lattice constants. Similarly, the features around $\hbar\omega$ = 5 eV in the reflectance spectra shifted towards the high photon energy. For the calculated IR spectrum of marcasite-type RhN_2, the transitions corresponding to the hump structure in RuN_2 are located lower than ~1 eV, i.e., the hump around $\hbar\omega$ = 0.5 eV in the absorption spectrum of RhN_2. In addition to this shift, the band gap at $E_B \approx -1.1$ eV in the conduction band region may induce the steep reduction of the reflectance and absorption at $\hbar\omega$ = 1–2 eV. Thus, the existence of the band gap in the conduction-band region and the weaker absorption of marcasite-type RhN_2 than that of RuN_2 might cause the weak Raman observation in the marcasite RhN_2.

The measured reflectance spectrum of marcasite-type RuN_2 is similar to the calculated spectrum, although the hump structure is observed at lower photon energy than the calculated value, and the reflectance values are slightly different from the predicted values. In marcasite-type RhN_2, a large discrepancy is recognized between $\hbar\omega$ = 0.2 and 1 eV. This suggests the presence of additional excitations, which are not included in the calculation, such as a phonon, or a shift of the above-mentioned Rh d-p transitions towards the high photon energy.

4. Conclusions

We measured the IR reflectance spectra of marcasite-type RuN_2 and RhN_2, arsenopyrite-type IrN_2, and pyrite-type PtN_2, which showed qualitative agreement with the predicted electric properties and reasonable agreement with the calculated reflectance spectra. Observation of weak Raman signals for marcasite-type RhN_2 may be attributed to the existence of the band gap in the conduction bands in contrast to marcasite-type RuN_2.

Acknowledgments

This research was partly supported by JSPS KAKENHI (Grant Nos. 25289219 and 16H02388). The IR reflectance measurements were performed with the BL43IR beamlines at

SPring-8 with the approval of the Japan Synchrotron Radiation Research Institute (Proposal Nos. 2015A1164, 2016A1074, and 2017A1147).

* Corresponding author: E-mail: j45880a@cc.nagoya-u.ac.jp

[1]Present address: *Department of Material Physics, Graduate School of Engineering, Nagoya University, Furo-cho, Chikusa-ku, Nagoya 464-8603, Japan.*

[1] P. F. McMillan, New materials from high-presure experiments, Nature Mater. **1** (2002) 19–25.

[2] M. Imada, A. Fujimori, Y. Tokura, Metal insulator transitions, Rev. Mod. Phys. **70** (1998) 1039–1263.

[3] X. Wang, A. M. Turner, A. Vishwanath, S. Y. Savrasov, Topological semimetal and Fermi-arc surface sates in the electronic structure, Phys. Rev. B **83** (2011) 205101-1–9.

[4] H. Weng, C. Fang, Z. Fang, B. A. Bernevig, X. Dai, Weyl semimetal phase in noncentrosymmetric transition-metal monophosphides, Phys. Rev. X **5** (2015) 011029-1–10.

[5] S. Souma, Z. Wang, H. Kotaka, T. Sato, K. Nakayama, H. Kimizuka, T. Takahashi, K. Yamauchi, T. Oguchi, K. Segawa, Y. Ando, Direct observation of nonequivalent Fermi-arc states of opposite surfaces in the noncentrosymmetric Weyl semimetal NbP, Phys. Rev. B **93**, (2016) 161112(R)-1–6.

[6] M. Z. Hasan, C. L. Kane, colloquium: Topological insulators, Rev. Mod. Phys. **82** (2010) 3045–3067.

[7] X.-L. Qi and S. C. Zhang, Topological insulators and superconductors, Rev. Mod. Phys. **83** (2011) 1057–1110.

[8] K. Niwa, K. Suzuki, S. Muto, K. Tatsumi, K. Soda, T. Kikegawa, M. Hasegawa, Discovery of the last remaining binary platinum-group pernitride RuN_2, Chem. Eur. J. **20** (2014) 13885–13888.

[9] K. Niwa, D. Dzivenko, K. Suzuki, R. Riedel, I. Troyan, M. Eremets, M. Hasegawa, High pressure synthesis of marcasite-type rhodium pernitride, Inorg. Chem. **53** (2014) 697–699.

[10] E. Gregoryanz, C. Sanloup, M. Somayazulu, J. Badro, G. Fiquet, H.-K. Mao, R. J. Hemley, Synthesis and characterization of a binary noble metal nitride, Nat. Mater. **3** (2004) 294–297.

[11] A. F. Young, J. A. Montoya, C. Sanloup, M. Lazzeri, E. Gregoryanz, S. Scandolo, Interstitial dinitrogen makes PtN_2 and insulationg hard solid, Phys. Rev. B **73** (2006) 153102-1–4.

[12] A. F. Young, C. Sanloup, E. Gregoryanz, S. Scandolo, R. J. Hemley, H.-K. Mao,

Synthesis of novel metal nitrides IrN_2 and OsN_2, Phys. Rev. Lett. **96** (2006) 155501-1–4.

[13] R. Yu, Q. Zhan, L. C. de Jonghe, Crystal structures of and displacive transitions in OsN_2, IrN_2, RuN_2, and RhN_2, Angew. Chem. Int. Ed. **46** (2007) 1136–1140.

[14] J. A. Montoya, A. D. Hernandez, C. Sanloup, E. Gregoryanz, S. Scandolo, OsN2: Crystal structure and electronic properties, Appl. Phys. Lett. **90** (2007) 011909-1–3.

[15] E. R. Hernandez, E. Canadell, Marcasite vs. arsenopyrite structural choice in MN_2 (M = Ir, Os and Rh) transition metal nitrides, J. Mater. Chem. **18** (2008) 2090–2095.

[16] K. Soda, T. Mizui, M. Komabuchi, M. Kato, T. Terabe, K. Suzuki, K. Niwa, Y. Shirako, M. Hasegawa, M. Akaogi, H. Kojitani, E. Ikenaga, Microbeam hard X-ray photoemission study on platinum-group metal pernitrides, J. Phys. Soc. Jpn. **86** (2017) 064804-1–5.

[17] H. Okamura, Y. Ikemoto, T. Moriwaki, and T. Nanba, Infrared spectroscopy techniques for studying the electronic structures of materials under high pressure, J. J. Appl. Phys. **56** (2017) 05FA11-1–8.

[18] G. J. Piermarini, S. Block, J. D. Bamett, R. A. Forman, Calibration of the pressure dependence of the R1 ruby fluorescence line to 195 kbar, J. Appl. Phys. **46** (1975) 2774–2780.

[19] H. K. Mao, P. M. Bell, J. W. Shner, D. J. Steinberg, J. Appl. Phys. 49 (1978) 3276–3283.

[20] J. P. Perdew, K. Burke, M. Ernzerhof, Generalized gradient approximation made simple, Phys. Rev. Lett. **77** (1996) 3865–3868.

[21] P. Blaha, K. Schwarz, P. Sorantin, S. B. Trickey, Full-potential, linearized augmented plane wave programs for crystalline systems, Comput. Phys. Commun. **59**, 399 (1990) 399–415.

[22] P. Blaha, K. Schwarz, G. Madsen, D. Kvasnicka, J. Luitz, *An Augmented Plane Wave + Local Orbitals Program for Calculating Crystal Properties rev. ed.* (Vienna Univ. of Tech., Wien, Austria, ISBN 3-9501031-1-2, 2013).

[23] K. Glantschnig and C. Ambrosch-Draxl, Relativistic effects on the linear optical properties of Au, Pt, Pb and W, New J. Phys. **12** (2010) 103048-1–16.

[24] C. Ambrosch-Draxl, J. O. Sofo, Linear optical properties of solids within the full-potential linearized augmented planewave method, Comp. Phys. Commun. **175** (2006) 1–14.

[25] H. Wang, Y. Chen, Y. Kaneta, S. Iwata, First-principles investigation of structural, electronic and optical properties of IVA group spinel nitrides, Eur. Phys. J. B **59** (2007) 155–165.

[26] F. Tran, P. Blaha, Accurate band gaps of semiconductors and insulators with a semilocal exchange-correlation potential, Phys. Rev. Lett. **102** (2009) 226401-1–4.

[27] A. Kuzmenko, RefFIT software to fit optical spectra, http://optics.unige.ch/Alexey/refit.html.

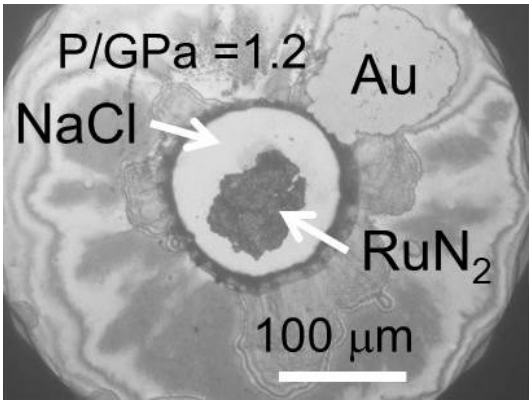

Fig. 1. RuN_2 specimen in a diamond anvil cell for the reflectance measurement under high pressure. Reference Au was placed on a metal (stainless steel) gasket beside the specimen. A small ruby ball (not indicated) was also mounted for the pressure measurement. NaCl was added with as a pressure-transmitting medium for this specimen after recovery to ambient pressure.

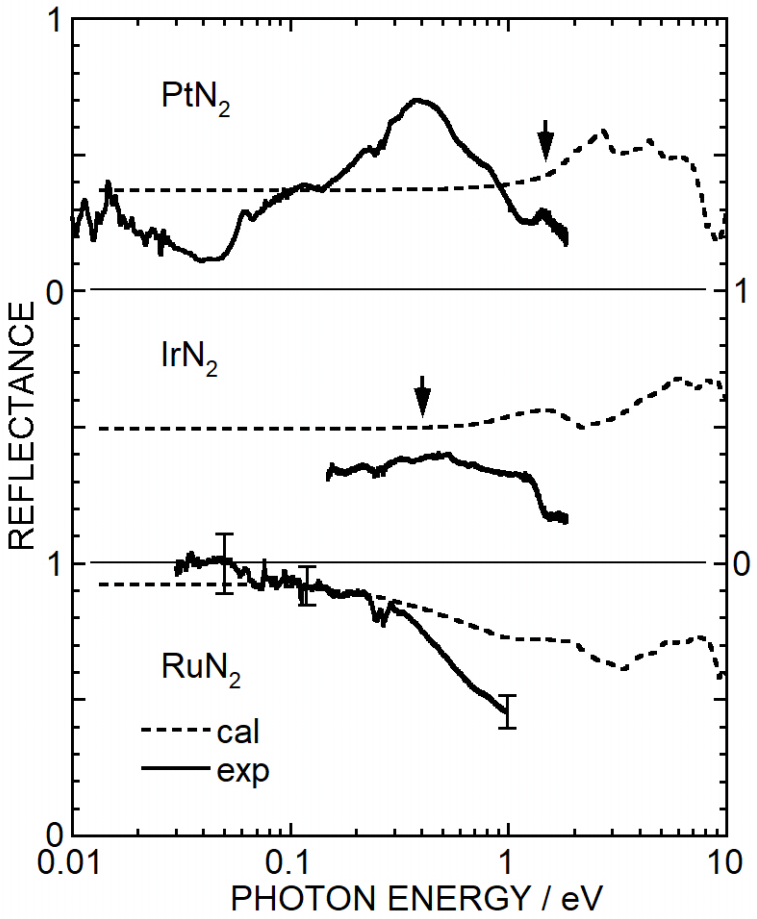

Fig.2. Measured and calculated reflectance spectra of marcasite-type RuN_2, arsenopyrite-type IrN_2, and pyrite-type PtN_2 at ambient pressure. Arrows indicate calculated band gap energies. Typical errors are indicated for RuN_2.

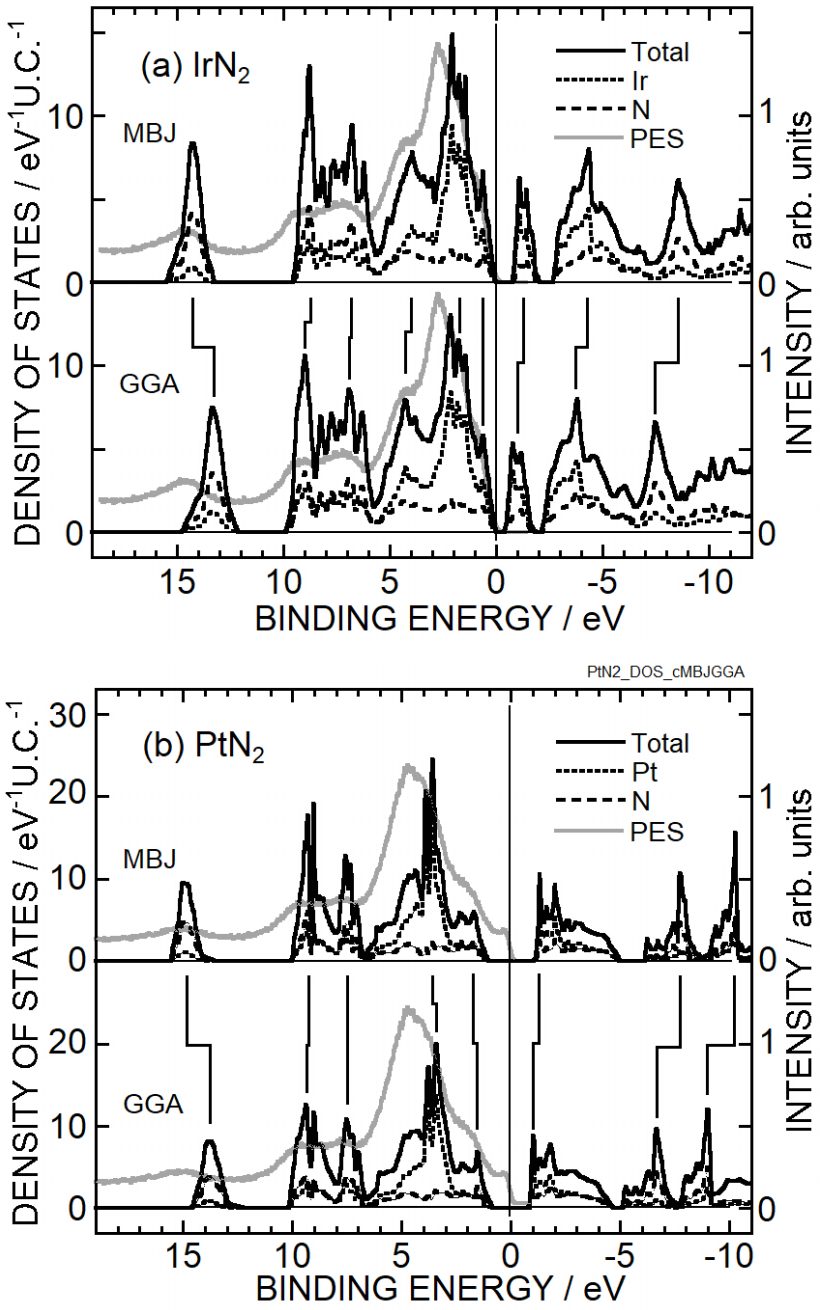

Fig.3. Electronic densities of states (DOSs) calculated using the modified Becke–Johnson (MBJ) potential and the generalized gradient approximation (GGA) for (a) arsenopyrite-type IrN_2 and (b) pyrite-type PtN_2. Total DOSs are shown by black solid curves, and the constituent transition-metal and nitrogen partial DOSs are presented by dotted and broken curves, respectively. Experimental hard X-ray photoelectron spectra (ref. 16) are also shown by gray curves for comparison. The origin of the binding energy is set to the experimental Fermi energy of the metallic reference Au. The DOSs are plotted so that the occupied valence band tops and the centers of the band gap are aligned to the Fermi energy for IrN_2 and PtN_2, respectively. Linked vertical bars indicate the corresponding bands for both calculations.

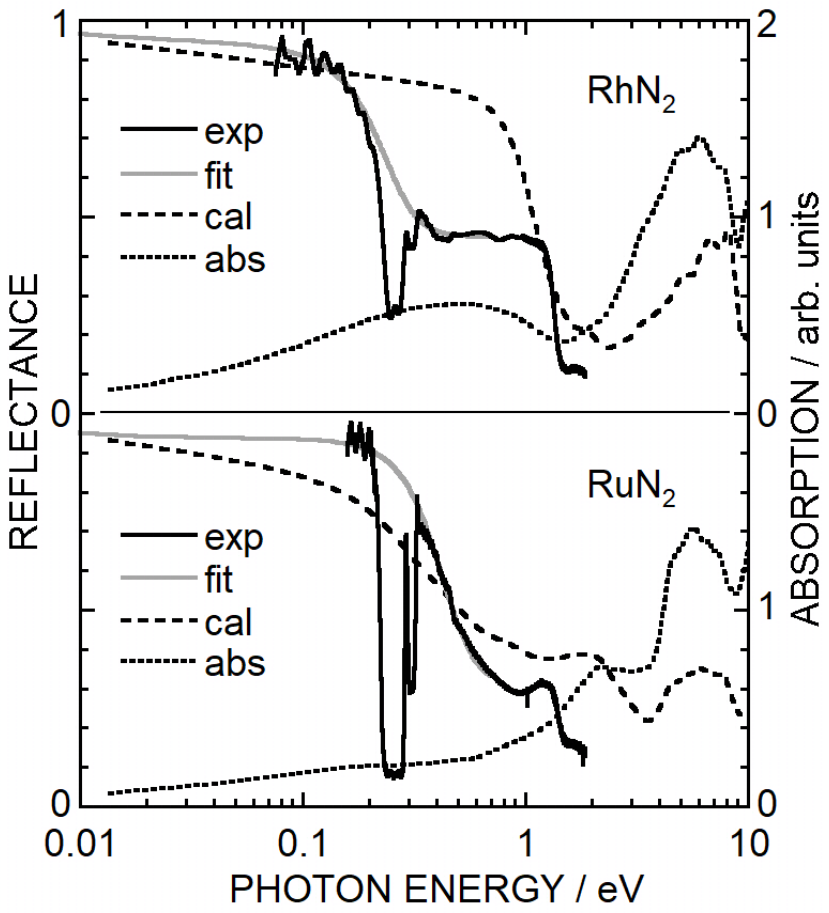

Fig. 4. Reflectance spectra (solid curves; exp) of marcasite-type RuN_2 and RhN_2 under high pressures of 28 and 33 GPa, respectively. For comparison, broken (cal) and gray (fit) curves show spectra obtained from the calculated electronic band structures and by fitting Drude–Lorentz model responses to the experimental data, respectively. Calculated absorption spectra are also shown by dotted curves.

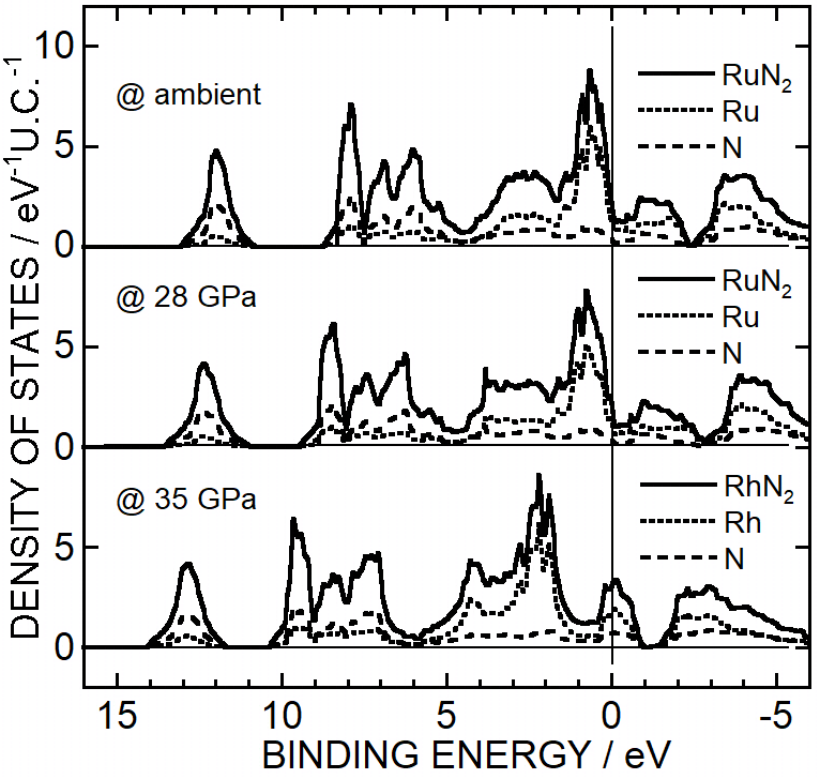

Fig. 5. Density of states (DOSs) calculated for marcasite-type RuN_2 and RhN_2. Total DOSs and partial DOSs of the constituent transition-metals Ru or Rh and N are shown by solid, dotted, and broken curves, respectively.

Table 1. Lattice constants used in the present calculation at various pressures, bulk moduli B_0 and its pressure derivative B'_0 at 0 GPa (ambient pressure) for marcasite-type RuN_2 [9] and RhN_2 [8]. The 4g Wyckoff positions of nitrogen in marcasite-type RuN_2 and RhN_2 are fixed at (0.123, 0.408, 0) and (0.124, 0.413, 0), respectively [13].

	P/GPa	*a*/pm	*b*/pm	*c*/pm	B_0	B'_0
RuN_2	0	407.3	488.8	270.7	330	4.1
	28	400.3	478.3	261.6		
	43	395.9	473.8	258.5		
RhN_2	0	398.2	485.8	283.4	235	5.9
	35	388.1	470.8	271.1		
	43	384.7	468.3	269.6		

Table 2. Fitting parameters of Drude-Lorentz model for RuN_2 and RhN_2.

	ε_∞	$\hbar\omega_{PD}$/eV	$\hbar\gamma_D$/eV	$\hbar\omega_0$/ eV	$\hbar\omega_{PL}$/eV	$\hbar\gamma_L$/eV
RuN_2	87.5	5.23	0.0449	0.665	6.78	1.40
RhN_2	195	5.60	0.127	0.665	4.59	0.609